Geophysical Journal International

Geophys. J. Int. (2019) **218,** 1210–1225
Advance Access publication 2019 May 17
GJI Geomagnetism, Rock Magnetism and Palaeomagnetism

doi: 10.1093/gji/ggz233

Equatorially trapped waves in Earth's core

Bruce Buffett[1] and Hiroaki Matsui[2]

[1]*Department of Earth and Planetary Science, University of California, Berkeley, CA* 94720*, USA. E-mail: bbuffett@berkeley.edu*
[2]*Department of Earth and Planetary Sciences, University of California, Davis, CA* 95616*, USA*

Accepted 2019 May 16. Received 2019 April 18; in original form 2019 February 7

SUMMARY

Short-period fluctuations in geomagnetic acceleration are detected in recent satellite observations. A major component of this signal is confined to the equatorial region, suggesting the presence of equatorial waves, but the precise nature of these waves is not known. We explore the possibility that these waves arise from an interplay of magnetic, Archimedes and Coriolis forces in a stratified layer at the top of the core (sometimes called MAC waves). We adopt a beta-plane approximation and show that low-frequency MAC waves are not trapped near the equator when the root-mean-square (rms) radial magnetic field is constant over the surface of the core–mantle boundary. However, equatorial trapped MAC waves emerge when the rms radial magnetic field increases towards the poles. Further confinement of MAC waves occurs when we account for the leading-order effects of spherical geometry. The resulting MAC waves propagate to the east with phase velocities that depend strongly on the thickness of the stratified layer. Waves with periods less than 10 yr are predicted when the layer thickness is less than 30 km. These waves have low quality factors, $Q \approx 1$, which means that they propagate only a few thousand kilometers before being dissipated by ohmic losses. Evidence for eastward and westward propagating disturbances in the observations may reflect a superposition of wave propagation and forced motion by an excitation source. Separation of the source from the wave propagation may be possible if the source is due mainly to westward drifting plumes in the equatorial region.

Key words: core; rapid time variations; satellite magnetics.

1 INTRODUCTION

Observations of the geomagnetic field offer a wealth of information about the dynamics of Earth's core. Historical records from the past 400 yr (Jackson *et al.* 2000) have been used to construct models for the geomagnetic field and its first time derivative. Satellite-based data have improved these models (Olson *et al.* 2006; Lesur *et al.* 2008) and expanded their scope to include estimates of the second time derivative (sometimes called geomagnetic acceleration). With these advances come new opportunities to explore the dynamics of Earth's core on short timescales. Pulses of geomagnetic acceleration have been reported in equatorial (Chulliat *et al.* 2010) and polar regions (Finlay *et al.* 2016) with durations as short as a few years.

Detecting short-period dynamics is difficult with only the first time derivative because most of this signal can be explained with a steady flow (e.g. Bäerenzung *et al.* 2018). Deviations from a steady flow are most evident at periods of several decades or more. A well documented example involves time variations in the zonal part of the flow (Jackson 1997), which contributes to detectable changes in the length of day (Jault *et al.* 1988; Jackson *et al.* 1993). Adding information from geomagnetic acceleration enables similar studies on much shorter timescales. To illustrate we show a snapshot of geomagnetic acceleration from the CHAOS-6 model (Finlay *et al.* 2016) in 2003 (see Fig. 1). A train of pulses in geomagnetic acceleration is evident below the Indian Ocean between the equator and 30° S. The most prominent features appear to be confined in longitude and they are generally short-lived. Other disturbances are reported below the equatorial region of South America, notably in 2014. Some of these features propagate to the east (Chulliat *et al.* 2010), while others propagate to the west (Finlay & Jackson 2003; Kloss & Finlay 2019). In some instances the velocity of the disturbance exceeds the largest fluid velocities in the core. Processes other than fluid advection must be responsible, and waves may offer one explanation (Aubert 2018).

A quantitative description of short-period waves is a necessary starting point for any attempt to interpret geomagnetic acceleration. Several prior studies of magnetic waves in rapidly rotating fluids (Canet *et al.* 2014; Hori *et al.* 2015; Labbe *et al.* 2015) have relied on the quasi-geostrophic approximation to enforce the condition of rapid rotation. These studies adopt large-scale magnetic fields and predict waves with periods of 10^2 to 10^3 yr. Much more rapid fluctuations are evident in models of geomagnetic acceleration, motivating a search for other types of waves. Suggestions of fluid stratification at the top of the core enable a type of wave

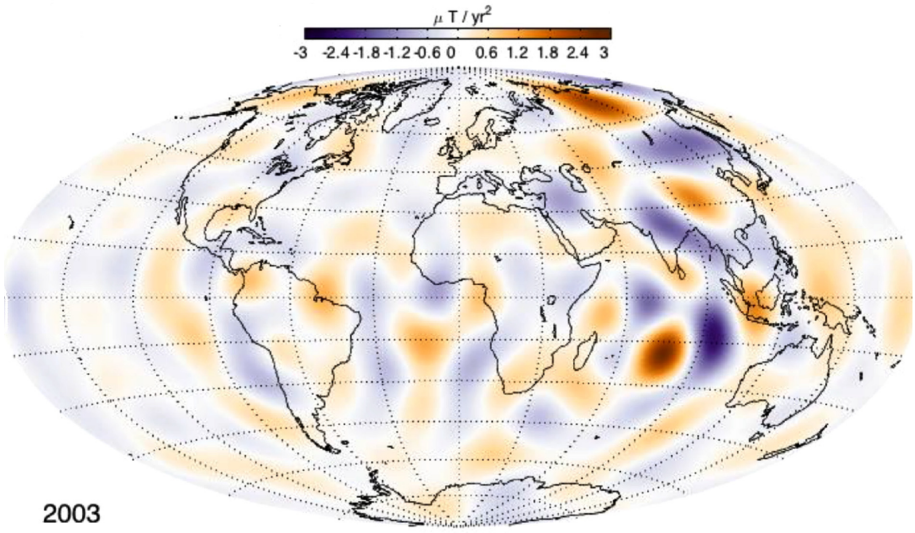

Figure 1. Geomagnetic acceleration at the core–mantle boundary from the CHAOS-6 model (Finlay *et al.* 2016). Short-lived pulses of geomagnetic acceleration are detected in the equatorial and polar regions (from http://www.space-center.dk).

known as Magnetic-Archimedes-Coriolis (MAC) waves (Bergman 1993; Braginsky 1993). These waves can have periods of 10 yr or less, depending on the local conditions. The goal of this study is to develop a physical model for equatorially trapped MAC (eMAC) waves with the aim of explaining observations of short-period geomagnetic acceleration in the equatorial region.

A common strategy for dealing with equatorial waves in oceanographic and atmospheric applications is based on the equatorial beta-plane (e.g. Pedlosky 2003). This approach has been used to describe equatorial Rossby waves, which are trapped near the equator by gradients in the Coriolis force. An equatorial beta-plane has also been applied to the case of magnetic Rossby waves (Bergman 1993). However, the standard approach does not work for low-frequency eMAC waves, at least under general conditions. One important and relevant exception occurs when there are strong gradients in the magnetic force away from the equator. A sufficiently strong gradient in the magnetic force can cause equatorially trapping of low-frequency MAC waves in much the same way as gradients in the Coriolis force produce equatorial Rossby waves. Apart from this somewhat restrictive case, a reliable description of the waves must retain the influences of spherical geometry. We show that the required extensions can be represented in the form of a power series expansion in the meridional coordinate. Each additional term in the series extends the validity of the solution away from the equator. Good agreement with a general numerical solution (Knezek & Buffett 2018) is achieved with only one or two additional terms. The main advantage of the approach described here is that it substantially reduces the computational cost, making it practical to use as a forward model in inversions of geomagnetic acceleration. It also greatly simplifies the connection between the wave properties and the local conditions near the core–mantle boundary.

We begin with a brief description of MAC waves in Section 2 before introducing the power series expansion in the meridional coordinate in Section 3. Truncating the expansion at the linear term gives the standard beta-plane approximation. Extending the series expansion to include quadratic terms accounts for the leading-order effects of spherical geometry. In many instances the quadratic terms are enough to give good agreement with previous numerical results, although it is straightforward to add higher order terms. The model is used in Section 4 to explore the conditions required for rapid changes in geomagnetic acceleration, followed by a brief discussion in Section 5 of strategies to recover wave parameters from models of geomagnetic acceleration.

2 DESCRIPTION OF MAC WAVES IN A THIN STRATIFIED LAYER

Global-scale waves in a shallow layer have a short vertical length scale relative to the horizontal wavelength. Restrictions imposed on the velocity field by the continuity condition mean that the vertical velocity is roughly a factor of H/L smaller than the horizontal velocity, where H is the layer thickness and L is the wavelength. A typical wavelength is $L = 3000$ km (Chulliat *et al.* 2015), whereas the layer thickness considered here varies from $H = 20$ to 100 km. (We extend the range to include thin layers because they are more compatible with short period of geomagnetic acceleration). Weak vertical flow causes only small departures from a vertical hydrostatic balance, so it is customary to enforce hydrostatic equilibrium. However, the vertical motion is sufficient to disturb the density field when the fluid is stably stratified, causing pressure perturbations and a large-scale horizontal flow in the presence of rapid rotation.

It is also common to retain only the radial component of the rotation vector in the Coriolis term (Pedlosky 1987) because a leading-order hydrostatic balance in the vertical direction means that the horizontal component of rotation vector only enters the dynamics through the radial velocity. Even though the Coriolis term vanishes on the equator, the increase with latitude is rapid enough to ensure that the horizontal component of rotation is negligible beyond a degree or two of the equator. When waves extend much further from the equator we expect the horizontal component of rotation to have a small role. This expectation is supported by direct calculations for the case of zonal MAC waves (Buffett 2014).

Waves are treated as small perturbations on a background state, which is defined by a velocity $\mathbf{V}_0$, magnetic field $\mathbf{B}_0$, pressure $\tilde{P}_0$ and density ρ_0. The perturbations are denoted by $\mathbf{v}$, $\mathbf{b}$, p and ρ_1, respectively, and their governing equations are linearized about the background state. Various nonlinear terms, like the Lorentz force in the momentum equation, have the general form, $\mathbf{B}_0 \cdot \nabla \mathbf{b} + \mathbf{b} \cdot \nabla \mathbf{B}_0$.

The first term is always much larger than the second when the (vertical) length scale for the perturbation is much shorter than the length scale of the background magnetic field. Other nonlinear terms are handled in a similar way. For a static background velocity, the linearized momentum equation for perturbed velocity is given by

$$\partial_t \mathbf{v} + 2\boldsymbol{\Omega} \times \mathbf{v} = -\frac{1}{\rho_0}\nabla p + \frac{1}{\rho_0 \mu}\mathbf{B}_0 \cdot \nabla \mathbf{b} + \frac{\rho_1}{\rho_0}\mathbf{g}, \tag{1}$$

where ∂_t denotes differentiation with respect to time, $\boldsymbol{\Omega}$ is the rotation vector, μ is the permeability of free space and $\mathbf{g} = -g\hat{\mathbf{r}}$ is acceleration due to gravity (assumed to be solely in the radial direction $\hat{\mathbf{r}}$). The absence of viscous forces in (1) is justified by the small fluid viscosity in the liquid core (de Wijs *et al.* 1998; Ichikawa & Tsuchiya 2015).

Conservation of mass for an incompressible fluid defines the time dependence of the density perturbation,

$$\partial_t \rho_1 = -\mathbf{v} \cdot \nabla \rho_0 = -v_r \partial_r \rho_0, \tag{2}$$

where v_r is the radial velocity and ∂_r denotes differentiation with respect to radius r. An incompressible fluid requires the velocity field to obey the continuity condition, $\nabla \cdot \mathbf{v} = 0$. When the fluid layer is thin relative to the core radius R (i.e. $H/R << 1$) we can approximate the continuity condition in spherical coordinates (r, θ, λ) using

$$\partial_r v_r + \frac{1}{R\sin\theta}\partial_\theta(v_\theta \sin\theta) + \frac{1}{R\sin\theta}\partial_\lambda v_\lambda = 0, \tag{3}$$

where θ is colatitude and λ is longitude. The angle $\phi = \pi/2 - \theta$ is reserved to define the latitude.

The magnetic perturbation is governed by the linearized magnetic induction equation

$$\partial_t \mathbf{b} = \mathbf{B}_0 \cdot \nabla \mathbf{v} + \eta \nabla^2 \mathbf{b}, \tag{4}$$

where $\eta = (\mu\sigma)^{-1}$ is the magnetic diffusivity of the fluid and σ is the electrical conductivity. Gauss's law, $\nabla \cdot \mathbf{b} = 0$, is also imposed on the magnetic perturbation, although it is not explicitly used in the construction of the wave model.

Eqs (1)–(4) describe the waves subject to boundary conditions on the upper and lower surfaces of the layer. The fluid region below the stratified layer is taken to be stationary, which means that horizontal motion at the base of the layer is opposed by the effects of magnetic friction. We approximate this condition by letting $v_\theta = v_\lambda = 0$ at $r = R - H$. We also assume that the radial velocity vanishes at the core–mantle boundary ($r = R$). Pseudo-vacuum conditions are imposed on the magnetic perturbation at the core–mantle boundary, requiring $b_\theta = b_\lambda = 0$. These conditions are justified on the basis of the dynamics (Braginsky 1993), but a finite mantle conductivity can affect the detection of short-period magnetic fluctuations at the Earth's surface. Magnetic conditions at the base of the layer are even more complicated, but simplifications are possible if the conducting fluid underneath the layer is stationary. Any magnetic perturbation at the base of the layer diffuses into the underlying fluid over a magnetic skin depth. Consequently, the perturbations b_θ and b_λ are expected to vanish below the skin depth. It is reasonable to impose this condition at the base of the layer when the skin depth is short relative to the thickness of the layer.

Steep vertical gradients in the perturbations permit one final approximation in the governing equations. The largest contribution to terms like $\mathbf{B}_0 \cdot \nabla \mathbf{b}$ is due to the vertical gradient in $\mathbf{b}$, which has a magnitude on the order of $\mathbf{b}/H$. By comparison, the horizontal gradient is roughly $\mathbf{b}/L$. When the vertical and horizontal components of $\mathbf{B}_0$ are comparable, as is often the case in geodynamo models (including the one considered below), we can attribute most of the Lorentz force to the radial component of $\mathbf{B}_0$. Even a modestly larger horizontal component of $\mathbf{B}_0$ is liable to have a small influence on the dynamics as long as the ratio H/L is sufficiently small. This means that the term $\mathbf{B}_0 \cdot \nabla \mathbf{b}$ can be approximated using $B_r \partial_r \mathbf{b}$, where B_r is the radial component of the background magnetic field. Similar arguments apply to the induction term in (4). The resulting components of the momentum equation in spherical coordinates are

$$\partial_r p = -\rho_1 g \tag{5}$$

$$\partial_t v_\theta - 2\Omega\cos\theta\, v_\lambda = -\frac{1}{\rho_0 R}\partial_\theta p + \frac{1}{\rho_0 \mu} B_r \partial_r b_\theta \tag{6}$$

$$\partial_t v_\lambda + 2\Omega\cos\theta\, v_\theta = -\frac{1}{\rho_0 R\sin\theta}\partial_\lambda p + \frac{1}{\rho_0 \mu} B_r \partial_r b_\lambda, \tag{7}$$

while the components of the induction equation can be written compactly as

$$(\partial_t - \eta\partial_r^2) b_\zeta = B_r \partial_r v_\zeta, \tag{8}$$

where ζ represents one of the three spherical components (either r, θ or λ). To proceed we successively eliminate the perturbation variables from the governing equations to leave a pair of differential equations for b_θ and b_λ. These equations serve as the starting point for the extended beta-plane approximation. The steps leading to these two equations are straightforward, so the details are deferred to the Appendix.

3 EXTENDED BETA-PLANE APPROXIMATION

The standard beta-plane approximation adopts a local Cartesian coordinate system (x_s, y_s, z_s), where x_s and y_s define the eastward and northward coordinates, and z_s is the vertical coordinate relative to some reference surface. The relevant governing equations are obtained from the general equations in spherical coordinates by expanding the trigonometric terms in power series. For example, the Coriolis parameter, $f = 2\Omega\cos\theta$, can be written in terms of latitude, ϕ, as

$$f = 2\Omega\sin\phi \approx 2\Omega\phi + \mathcal{O}(\phi^3), \tag{9}$$

where the higher order terms in ϕ are omitted. Similarly, we define the horizontal coordinates using

$$x_s = R\cos\phi(\lambda - \lambda_0) \approx R(\lambda - \lambda_0) + \mathcal{O}(\phi^2) \tag{10}$$

$$y_s = R\phi + \mathcal{O}(\phi^2), \tag{11}$$

where λ_0 defines the origin of the eastward coordinate. By retaining the linear terms in ϕ, and discarding all higher order terms, we account for the variations in the Coriolis parameter with latitude, but exclude all other aspects of the spherical geometry (see Pedlosky 2003, for details). The goal of the extended beta-plane approximation is to provide a systematic way of retaining some of these higher order terms.

To achieve this goal we transform the governing equations in Section 2 from spherical coordinates (r, θ, λ) to coordinates (z, y, λ), where the new meridional coordinate, y, is defined by

$$y = \cos\theta. \tag{12}$$

The same choice is made for the meridional coordinate in the studies of Zaqarashvili *et al.* (2007) and Marquez-Artavia *et al.* (2017). The vertical coordinate, $z = r - R$, is referenced to the core–mantle boundary. The wave equation is still expressed in terms of magnetic perturbations b_θ and b_λ, but we use y and z rather than θ and r to define the meridional and vertical positions. This choice means that $y = 0$ defines the equator and the poles occur at $y = \pm 1$. It also means that the Coriolis parameter is represented exactly as $f = 2\Omega y$. Converting the original equations to the new coordinates is simplified by defining new variables for the magnetic perturbation,

$$b'_\theta = (1-y^2)^{1/2}\, b_\theta \text{ and } b'_\lambda = (1-y^2)^{-1/2}\, b_\lambda. \tag{13}$$

When the waves are confined to the equator, and y is small, the difference between the new and the old variables is small. In fact there is no distinction for approximations that omit terms $\mathcal{O}(y^2)$ and higher. Higher order solutions are formulated in terms of b'_θ and b'_λ, so the transformation in (13) is used to convert these solutions back to the original variables before interpreting the results. Singularities at the poles are not a problem if the solutions are confined to the region of the equator (see below).

Solutions for the magnetic perturbation are sought in the form

$$b'_\theta(t,z,y,\lambda) = \tilde{b}'_\theta(y)\sin(kz)e^{i(m\lambda-\omega t)} \tag{14}$$

$$b'_\lambda(t,z,y,\lambda) = \tilde{b}'_\lambda(y)\sin(kz)e^{i(m\lambda-\omega t)}, \tag{15}$$

where m is the angular order, ω is the wave frequency and k is the vertical wavenumber. Boundary conditions on the magnetic perturbation require $k = j\pi/H$, for $j = 1, 2....$ Substituting (14) and (15) into the transformed equations for b'_θ and b'_λ, yields a pair of ordinary differential equations for the coefficients $\tilde{b}'_\theta(y)$ and $\tilde{b}'_\lambda(y)$. All of these details are included in the Appendix, so we simply state the final form of the equations for the y-dependent coefficients. From the Appendix we have

$$[\partial_y^2 - (M-I)(1-y^2)^{-1}]\tilde{b}'_\theta = Cy\, i\tilde{b}'_\lambda + im\partial_y\tilde{b}'_\lambda \tag{16}$$

$$[-m^2 - (M-I)(1-y^2)]\tilde{b}'_\lambda = -Cy\, i\tilde{b}'_\theta + im\partial_y\tilde{b}'_\theta, \tag{17}$$

where the three dimensionless parameters

$$C = \frac{2\Omega\omega k^2R^2}{N^2} \qquad I = \frac{\omega^2k^2R^2}{N^2} \qquad M = \frac{V_a^2k^4R^2}{\chi N^2} \tag{18}$$

define the importance of Coriolis forces, inertia and magnetic forces relative to buoyancy forces. Several of the terms in (18) are defined in the Appendix. Specifically, we require the buoyancy frequency,

$$N = \sqrt{-\frac{g}{\rho_0}\frac{\partial\rho_0}{\partial r}}, \tag{19}$$

the Alfven velocity based on B_r,

$$Va = \frac{B_r}{\sqrt{\rho_0\mu}}, \tag{20}$$

and a parameter,

$$\chi = 1 + \frac{i\eta k^2}{\omega}, \tag{21}$$

that characterizes the influence of magnetic diffusion. (In the absence of diffusion $\chi \to 1$.)

It is important to note that (16) and (17) are equivalent to the original equations in spherical coordinates from Section 2; they retain a complete description of the influence of spherical geometry. Our goal is to find approximate solutions to (16) and (17) that include only the leading-order effects of the spherical geometry. To illustrate the general approach, it is helpful to start with the standard beta-plane approximation by omitting terms $\mathcal{O}(y^2)$ and higher.

3.1 Standard beta-plane approximation

The standard beta-plane approximation is recovered from (16) and (17) by dropping terms $\mathcal{O}(y^2)$ and higher. This truncation eliminates all terms connected with the spherical geometry, but retains the linear dependence due to the Coriolis term. It also removes any distinction between the original magnetic perturbation (b_θ, b_λ) and the modified quantities (b'_θ, b'_λ). The governing equations from (16) and (17) simplify to

$$[\partial_y^2 - (M-I)]\tilde{b}_\theta = Cy\, i\tilde{b}_\lambda + im\partial_y\tilde{b}_\lambda \tag{22}$$

$$[-m^2 - (M-I)]\tilde{b}_\lambda = -Cy\, i\tilde{b}_\theta + im\partial_y\tilde{b}_\theta, \tag{23}$$

where the y-dependent coefficients $(\tilde{b}'_\theta, \tilde{b}'_\lambda)$ are replaced with the coefficients for the original magnetic perturbation $(\tilde{b}_\theta, \tilde{b}_\lambda)$.

Rearranging the algebraic equation in (23) for $\tilde{b}_\lambda$ gives

$$\tilde{b}_\lambda = \frac{Cyi\tilde{b}_\theta}{m^2+M-I} - \frac{im\partial_y\tilde{b}_\theta}{m^2+M-I}, \tag{24}$$

which is then substituted into (22) to define a single wave equation for $\tilde{b}_\theta$. When M is treated as a constant (i.e. B_r^2 is constant over the core–mantle boundary), the resulting wave equation can be written in the form

$$\partial_y^2\tilde{b}_\theta - [\alpha_2\, y^2 - \alpha_0]\tilde{b}_\theta = 0, \tag{25}$$

where

$$\alpha_2 = \frac{C^2}{I-M}, \qquad \alpha_0 = -\frac{mC}{I-M} - m^2 + (I-M). \tag{26}$$

The general form of (25) offers insights into the origin of equatorial trapping. When y is small and α_0 is positive, we expect wave-like solutions in the meridional coordinate. However, when y is large and α_2 is positive, we expect a transition to exponential decay (or growth). Only solutions that vanish at large y are of interest here because we focus on waves that are trapped near the equator. The crucial point for equatorially trapped waves is the sign of α_2. It is always possible to change the sign of α_0 by changing the sign of the frequency, corresponding to a switch in the direction of propagation. Recall that C depends linearly on ω, so the sign of α_0 can depend on the direction of wave propagation, whereas the sign of α_2 does not.

From the expression for α_2 in (26) we can conclude that equatorially trapped waves on the standard beta plane require $I > M$. This result is consistent with the study of Bergman (1993), which showed that a strong magnetic field ($M > I$) could break the equatorial trapping of magnetic Rossby waves. (Trapping is a consequence of gradients in the Coriolis force away from the equator. Changes in the local wave speed with latitude act like a wave-guide for the propagation of Rossby waves). More generally we can expect any level of magnetic field to enable waves to escape from the wave guide if the frequency of those waves is low enough. From the definition of I and M in (18) the transition frequency is $\omega \approx V_a k$. As an example, consider a layer with $H = 100$ km ($k = \pi/H$) and a constant root-mean-square (rms) radial magnetic field of $B_r = 0.65$ mT ($V_a = 5.8\,\text{mm}\,\text{s}^{-1}$). The transition frequency is $1.8 \times 10^{-7}\,\text{s}^{-1}$, which

corresponds to a period of roughly 1 yr. Magnetic Rossby waves have much shorter periods, so the effects of inertia are large and these waves should be trapped near the equator.

Solutions of (25) for the frequency and structure of the waves can be viewed as an eigenvalue problem because discrete values for α_0 are required to ensure the solution vanishes as $y \to \infty$. A common practice in oceanography is to rescale the y coordinate to make $\alpha_2 = 1$ in the transformed equation. A solution that vanishes at $y \to \infty$ requires $\alpha_0 = 2n + 1$, for $n = 0, 1, 2....$ This restriction on α_0 is combined with the known functional form in (26) to determine the frequency. The spatial structure of the wave is described by a Hermite function in the rescaled coordinate y'. Thus the solution for $\tilde{b}_\theta(y')$ has the general form

$$\tilde{b}_\theta(y') = H_n(y')e^{-y'^2/2}, \tag{27}$$

where $H_n(y')$ is the Hermite polynomial of degree n. The first few polynomials are $H_0 = 1$, $H_1 = y'$ and $H_2 = 4y'2 - 2$.

Another method of solution is based on a direct formulation of (25) as an eigenvalue problem. Defining the operator

$$L = \partial_y^2 - \alpha_2 y^2 \tag{28}$$

allows us to write (25) in the form

$$\boldsymbol{L}\,\tilde{b}_\theta + \alpha_0 \boldsymbol{I}\,\tilde{b}_\theta = 0, \tag{29}$$

where $\boldsymbol{I}$ is the identity matrix and $\boldsymbol{L}$ is the discretized operator, evaluated using second-order central finite differences. (This makes $\boldsymbol{L}$ a tridiagonal matrix). Homogeneous boundary conditions at $y = 0$ and $y = \infty$ are directly incorporated into $\boldsymbol{L}$. In practice, the condition at $y = \infty$ is imposed by setting $\tilde{b}_\theta = 0$ at a large, but finite value of y. The choice of boundary condition at $y = 0$ is either $\partial_y \tilde{b}_\theta = 0$ or $\tilde{b}_\theta = 0$. The first choice gives symmetric solutions about $y = 0$, and corresponds to Hermite polynomials with even n. The other choice gives asymmetric solutions, corresponding to odd values of n. Once the eigenvalue α_0 is computed from (29), we compare it with the theoretical value in (26). Iterative adjustments to the wave frequency are used to bring these two values into agreement. Five or six iterations are usually enough when the waves are trapped near the equator. One advantage of the second approach is that it is easy to deal with complex frequencies in the presence of significant magnetic diffusion. We can also add higher order terms in y to the operator L (say y^4 terms) to extend the validity of the solution to higher latitudes.

Fig. 2 shows an example of the first two magnetic Rossby waves in a fluid layer with $H = 100$ km, $N = \Omega$ and $B_r = 0.65$ mT. Both of these waves propagate westward with periods of 21.1 d for $n = 0$ and 56.8 d for $n = 1$. (An angular order of $m = 6$ is adopted in both calculations). Because these waves are lightly damped by the effects of magnetic diffusion, the eigenfunctions for $\tilde{b}_\theta(y)$ are well approximated by (27). Low-frequency eMAC waves are not expected on the standard beta-plane when M is constant because $M > I$ at periods longer than about 1 yr. One exception (for constant M) occurs when the waves are heavily damped. In this case the wave-like and exponential behaviours are interchanged when the frequencies have large imaginary parts. This may be relevant for the study of Bergman (1993), which omitted the term $\mathbf{B}_0 \cdot \nabla \mathbf{v}$ from the induction equation and obtained purely imaginary frequencies.

3.2 Equatorial waves due to gradients in the radial magnetic field

A second type of wave guide occurs when the radial magnetic field increases towards the poles (Knezek & Buffett 2018). We quantify this effect on the standard beta-plane by allowing the magnetic parameter, $M(y)$, to vary with y. Here we focus on low-frequency eMAC waves because magnetic Rossby waves have frequencies that are too high to be detected in geomagnetic acceleration. Consequently, we drop the inertial effects by setting $I = 0$. This approximation incurs only a small error because the ratio of inertia to magnetic forces is roughly $I/M \approx 10^{-2}$ at typical frequencies for eMAC waves.

Returning to (22) and (23), we repeat the derivation of a single equation for $\tilde{b}_\theta$ when $M(y)$ is a function of y. The general form of the differential equation for $\tilde{b}_\theta$ is

$$\partial_y^2 \tilde{b}_\theta + \left[\frac{m^2 \partial_y M}{M(m^2+M)}\right]\partial_y \tilde{b}_\theta - (m^2+M)\tilde{b}_\theta + \frac{C^2}{M} y^2 \tilde{b}_\theta + \frac{mC}{M}\left[1 - \frac{y\partial_y M}{m^2+M}\right]\tilde{b}_\theta = 0. \tag{30}$$

We adopt a specific form for $M(y)$ using the output of a high-resolution geodynamo simulation, based on the *Rayleigh* code (Featherstone & Hindman 2016; Matsui *et al.* 2016). A snapshot of B_r at the core–mantle boundary is shown in Fig. 3. The longitudinally averaged value of B_r^2 generally increases towards the poles (see Fig. 4), although it includes a sharp drop near the north pole. The details of the magnetic field near the poles are not important when the waves are confined to the equator, so we approximate the large-scale variations in B_r^2 (and hence $M(y)$) using

$$M(y) = M(0)[1 + \Lambda^2 y^2], \tag{31}$$

which converts (30) into

$$\partial_y^2 \tilde{b}_\theta + \frac{2\Lambda^2 y}{1+\Lambda^2 y^2}\partial_y \tilde{b}_\theta + \left[\frac{C^2}{M(y)} y^2 + \frac{mC}{M(y)} - m^2\right]\tilde{b}_\theta = 0\,, \tag{32}$$

after dropping small terms due to $M/m^2 << 1$. Values for M/m^2 are nominally 10^{-3} to 10^{-2} at $m = 6$, depending on the thickness of the layer. Note that (32) reverts to the constant M case in (25) when $\Lambda^2 = 0$ and we drop the small M/m^2 terms. We can conclude that the main outcome of allowing $M(y)$ to vary is the appearance of a first-order derivative in the equation for $\tilde{b}_\theta$.

The first-order derivative in (32) can be eliminated by a procedure known as normalization (Lanczos 1996, pg. 368). We introduce a transformation

$$\tilde{b}_\theta = \frac{\tilde{b}''_\theta}{(1+\Lambda^2 y^2)^{1/2}}, \tag{33}$$

to define a new differential equation for the variable, $\tilde{b}''_\theta$,

$$\partial_y^2 \tilde{b}''_\theta - \left[\frac{\Lambda^2}{(1+\Lambda^2 y^2)} - \frac{C^2}{M(y)} y^2 - \frac{mC}{M(y)} + m^2\right]\tilde{b}''_\theta = 0, \tag{34}$$

where the first-order derivative has been removed. We can now express the differential equation for $\tilde{b}''_\theta$ in the form of (25) by expanding the coefficients in a power series about $y = 0$. Retaining only the second-order terms gives

$$\partial_y^2 \tilde{b}''_\theta - [\alpha_2 y^2 - \alpha_0]\tilde{b}''_\theta = 0, \tag{35}$$

where

$$\alpha_2 = -\frac{C^2}{M(0)} + \frac{mCr^2}{M(0)} - 2\Lambda^4, \qquad \alpha_0 = \frac{mC}{M(0)} - m^2 - \Lambda^2. \tag{36}$$

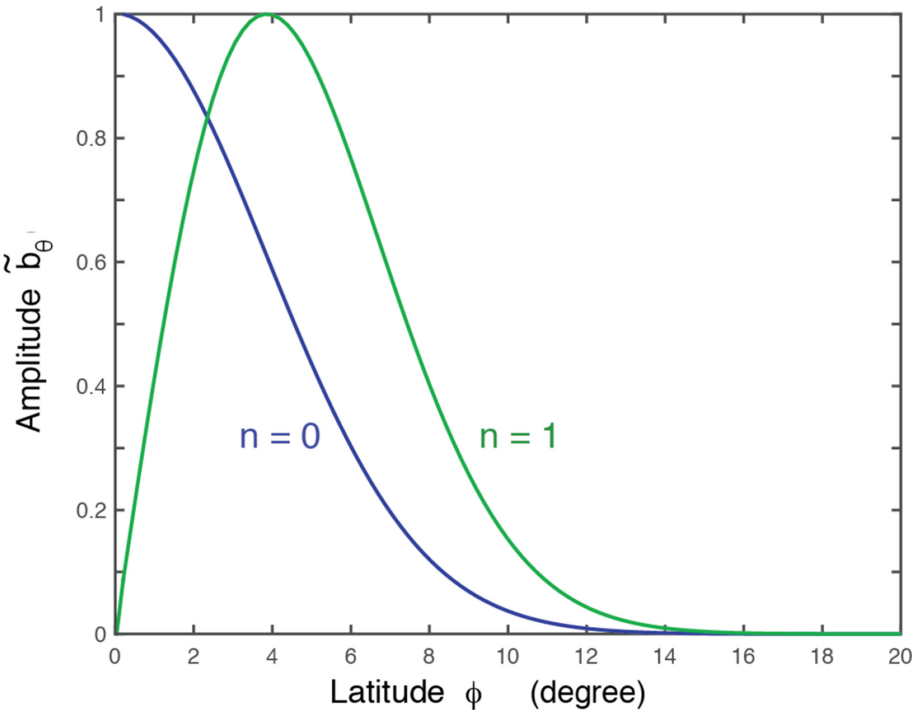

Figure 2. Amplitude of equatorially trapped magnetic Rossby waves as a function of latitude. The wave periods are 21.1 d for $n = 0$ and 56.8 d for $n = 1$. These waves are computed using $H = 100$ km, $N = \Omega$ and $B_r = 0.65$ mT (see the text).

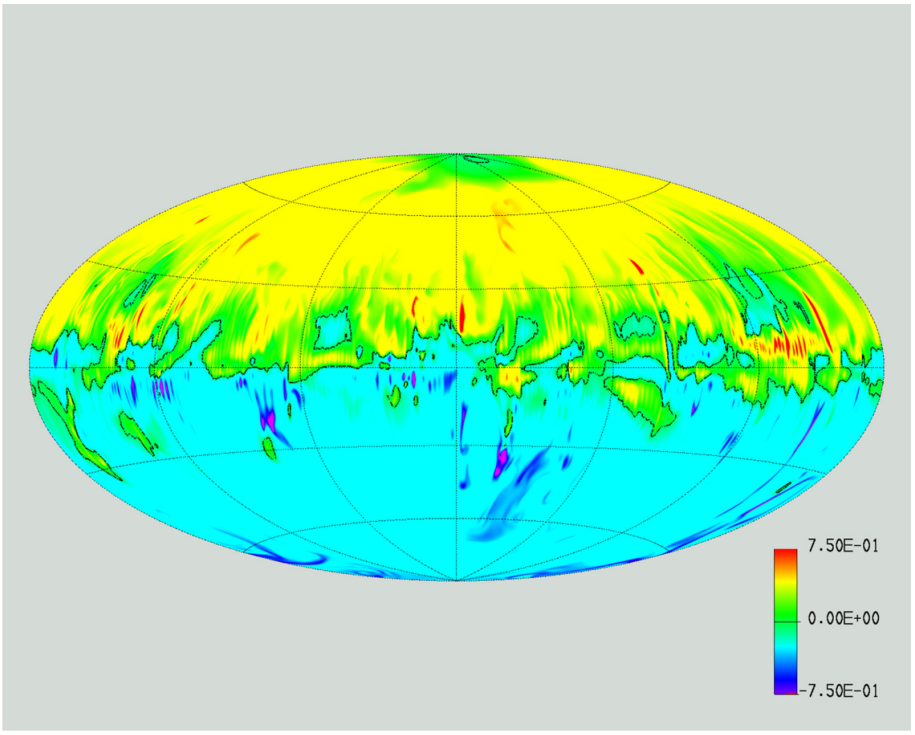

Figure 3. Radial magnetic field, B_r, at the core–mantle boundary from a numerical geodynamo model. The magnetic field is expressed in non-dimensional form using a characteristic scale $\sqrt{\rho_0 \mu \Omega \eta} = 0.854$ mT. The solution is computed on a mesh with (385, 768, 1536) gridpoints in the (r, θ, λ) directions. The non-dimensional control parameters include the Ekman number, $E = 10^{-6}$, the magnetic Prandlt number, $Pm = 0.5$, the Prandtl number, $Pr = 1$ and the Rayleigh number, $Ra = 3 \times 10^9$. Definitions follow the standard conventions in Christensen & Aubert (2006). The root-mean-square radial field over the surface of the core–mantle boundary is 0.24 mT.

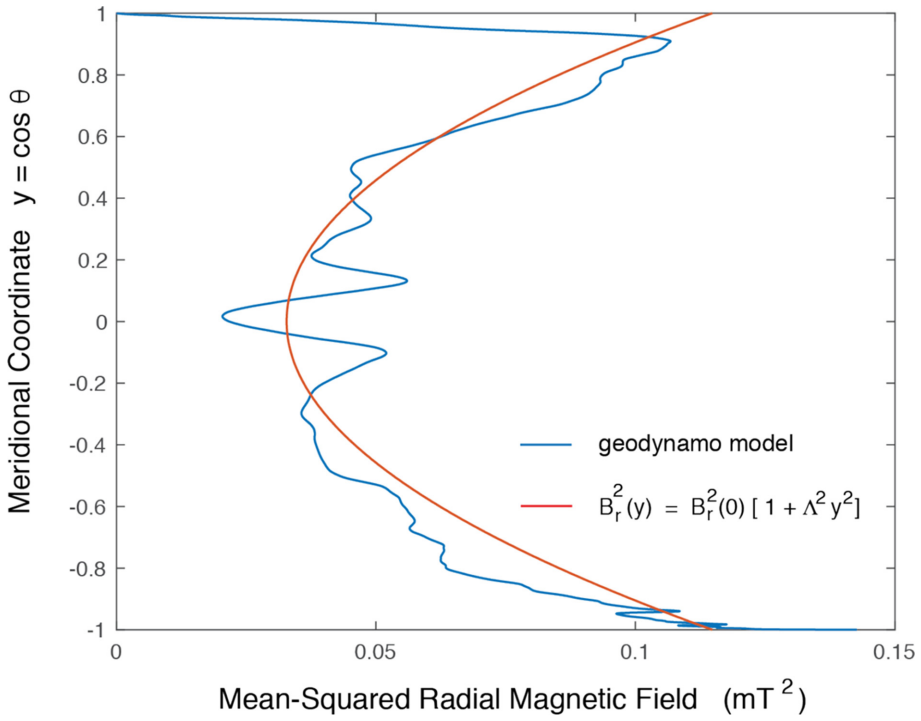

Figure 4. Mean-squared radial magnetic field, B_r^2, from the geodynamo model as a function of $y = \cos\theta$ (blue). The large-scale trend is approximated using a quadratic dependence on y (red). A weak radial magnetic field near the north pole ($y = 1$) has little influence on waves near the equator.

Including higher order terms in y extends the validity of the solution away from the equator.

Eq. (35) admits low-frequency eMAC waves because α_2 can be positive when C is positive. This condition requires positive frequencies or, equivalently, eastward propagating waves. Once a solution is found for $\tilde{b}''_\theta$, the transformation back to the original variable $\tilde{b}_\theta$ causes the wave amplitude to decrease away from the equator at a rate set by the value of Λ^2 (see eq. 33). Fitting the functional form in (31) to the longitudinally averaged value of B_r^2 in Fig. 4 gives an approximate value of $\Lambda^2 \approx 2.5$. We use this value below to quantify the change in M away from the equator.

The average amplitude of the radial field is treated as an adjustable parameter. The rms value of the radial magnetic field in the geodynamo model is $B_r^{rms} = 0.24$ mT for the snapshot shown in Fig. 3. This value is less than the estimate $B_r^{\rm rms} = 0.65$ mT, inferred from geodetic observations (Buffett *et al.* 2002; Koot *et al.* 2010). Consequently, we increase the strength of the magnetic field to match the geodetic constraint, but fix the spatial structure using $\Lambda^2 = 2.5$. Taking $B_r(0) = 0.48$ mT gives a spherically averaged value of $B_r^{\rm rms} = 0.65$ mT. A representative calculation using parameter values $H = 100$ km, $N = \Omega$ and $m = 6$ gives eastwards propagating waves with periods of 197.1 and 122.9 yr for the first symmetric ($n = 0$) and asymmetric ($n = 1$) waves, respectively. These periods are long compared with the transition period of roughly 1 yr, so the influences of inertia are small.

Fig. 5 shows the eigenfunctions for the original magnetic perturbation, $\tilde{b}_\theta(y)$, as a function of latitude. Both the $n = 0$ and $n = 1$ waves are confined to the vicinity of the equator by the gradient in the magnetic force. Changes in the local wave speed away from the equator act like a wave guide in much the same way that gradients in the Coriolis force alter the local propagation speed of Rossby waves. Lowering the gradient in M by reducing Λ^2 causes a decrease in the equatorial confinement of eMAC waves. Once Λ^2 is lowered to a value of 1 (not shown) the waves extend beyond the poles at $y = \pm 1$. This is not strictly a problem on a standard beta-plane because there are no poles when the influences of spherical geometry have been removed. Still, the results suggest that the gradient in the radial magnetic field must exceed a threshold to localize the waves near the equator. On the other hand, a non-zonal wave on a sphere must vanish at the poles to ensure that the solution is well defined. This suggests that the effects of spherical geometry should also limit meridional extent of the waves.

3.3 Influence of spherical geometry on equatorial waves

Eqs (16) and (17) retain a complete description of the spherical geometry in terms of the modified perturbations $\tilde{b}'_\theta$ and $\tilde{b}'_\lambda$. A direct solution for $\tilde{b}'_\theta$ and $\tilde{b}'_\lambda$ must vanish at the poles to ensure that this solution is well defined. Our goal here is to find a simpler, approximate solution that captures the leading-order effects of spherical geometry. The general approach follows the steps used previously in the standard beta-plane approximation. We first solve the algebraic equation in (17) for $\tilde{b}'_\lambda$ and substitute the result into (16). When the effects of inertia are omitted ($I = 0$), and the magnetic term, M, is treated as a constant, we obtain

$$(1-y^2)\partial_y^2\tilde{b}'_\theta - 2y\partial_y\tilde{b}'_\theta + \left[\frac{C^2y^2}{M} + \frac{mC}{M} - \frac{m^2}{1-y^2}\right]\tilde{b}'_\theta = 0 \quad (37)$$

after dropping small terms due to $M/m^2 << 1$.

Eq. (37) contains a first-order derivative, so we normalize this equation by introducing a transformation,

$$\tilde{b}'_\theta = \frac{\tilde{b}''_\theta}{\sqrt{1-y^2}}, \quad (38)$$

to obtain a differential equation for the new variable, $\tilde{b}''_\theta$,

$$\partial_y^2\tilde{b}''_\theta - \left[\frac{m^2-1}{(1-y^2)^2} - \frac{\mathcal{L}}{1-y^2}\right]\tilde{b}''_\theta = 0, \quad (39)$$

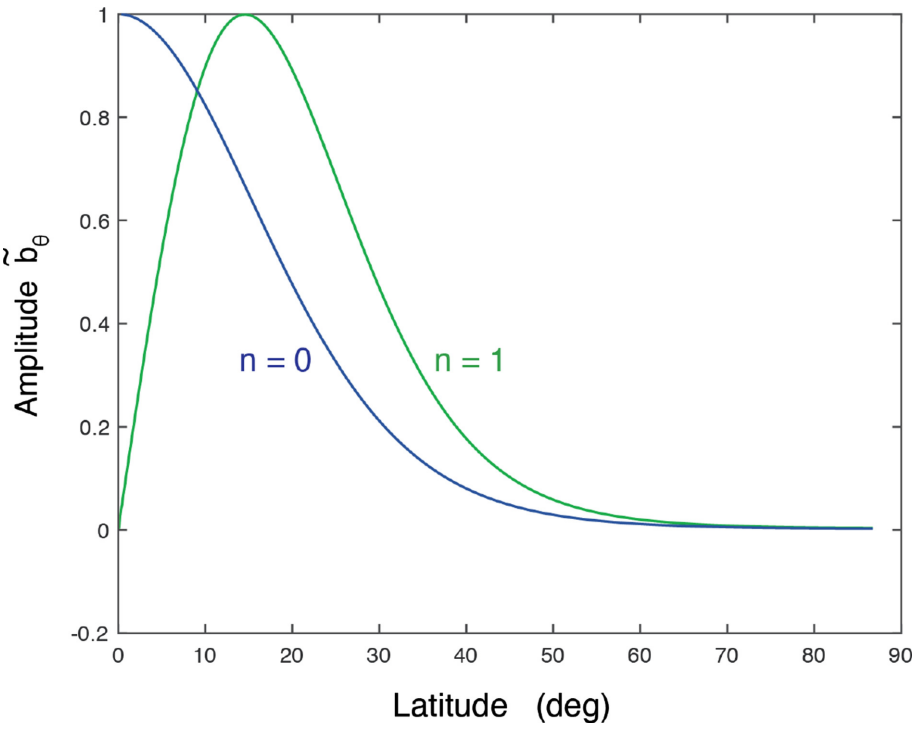

Figure 5. Amplitude of low-frequency eMAC waves as a function of latitude. Symmetric ($n = 0$) and asymmetric ($n = 1$) waves on the standard beta-plane are trapped near the equator by the influences of gradients in the radial magnetic field.

where

$$\mathcal{L} = \frac{C^2 y^2}{M} + \frac{mC}{M}. \tag{40}$$

In the final step we expand the coefficient in (39) in a power series about $y = 0$. Extending the series to include y^2 terms gives

$$\partial_y^2 \tilde{b}_\theta'' - (\alpha_2 y^2 - \alpha_0)\tilde{b}_\theta'' = 0, \tag{41}$$

where the coefficients are

$$\alpha_2 = -\frac{C^2}{M} - \frac{mC}{M} + 2(m^2 - 1), \quad \alpha_0 = \frac{mC}{M} - (m^2 - 1). \tag{42}$$

A positive term, $2(m^2 - 1)$, in the definition of α_2 permits equatorially trapped waves on the extended beta-plane. By comparison, equatorial MAC waves do not occur on a standard beta-plane when magnetic term M is constant.

The method of solution follows the approach used previously on the standard beta-plane. We look for solutions for $\tilde{b}_\theta''$ by formulating (41) as an eigenvalue problem for α_0. As before, the computed value for α_0 is compared with the predicted value in (42). Iterative adjustments to the frequency, ω, are used to bring the two values into agreement. Once we compute the eigenfunction, $\tilde{b}_\theta''$, we use the transformation in (38) to evaluate $\tilde{b}_\theta'$. A second transformation in (13) is required to recover the solution for the original variable (e.g. $\tilde{b}_\theta$). The singularity in these transformations at $y = \pm 1$ means that small errors in the solution are greatly amplified at the poles. One source of error is introduced by truncating the power series for the coefficient in (39). The wave amplitude may no longer vanish at the poles, so the transformations back to the original variables can cause a problem. To deal with this problem we represent the transformation in (38) as a power series

$$\frac{1}{\sqrt{1 - y^2}} = 1 + \frac{1}{2}y^2 + \frac{3}{8}y^4 + \ldots \tag{43}$$

and choose a truncation comparable to the value used in the differential equation. Here we truncate the approximate transformation after y^4. Using (43) to evaluate the transformation only affects the eigenfunction (see below), and leaves the wave frequency unchanged. The change in the eigenfunction becomes less important as the wave is more confined to the equator.

To illustrate this point we compute the first eMAC wave ($n = 0$) using $H = 100$ km, $N = \Omega$, $m = 6$, and a constant radial magnetic field $B_r = 0.65$ mT. The resulting wave propagates to the east with a period of 129.8 yr. Fig. 6 shows the eigenfunction for $\tilde{b}_\theta'$ computed using both the exact and approximate transformation. The two eigenfunctions agree very well in the equatorial region, but diverge close to the pole. Because the governing equation in (41) does not retain a full description of the spherical geometry, the solution may not converge to zero at $y = 1$. In this case the exact transformation causes a large error near the pole. This error is greatly reduced by using the approximate transformation, but the eigenfunction is largely unchanged in the equatorial region. Adding another term in the power series expansion (not shown) improves the convergence at $y = 1$, and reduces the error, but the spatial structure of the wave is not substantially altered away from the pole.

The eigenfunction for the second eMAC wave ($n = 1$) with constant M extends even further beyond the pole at $y = 1$ when we include only the y^2 terms in the series expansion. While these terms account for the leading-order effects of spherical geometry, the quadratic terms alone are not sufficient to ensure that the waves vanish at the poles. Small wave amplitudes at the poles introduce errors in the wave periods. Eq. (42) shows that the equatorial confinement of the waves depends entirely on m when M is constant. Low values for m allow the waves to extend beyond the poles, and even the choice of $m = 6$ for the $n = 0$ wave (see Fig. 6) is not sufficient to force the wave to vanish at the pole. The amplitude of the $n = 1$ wave is even larger at the pole.

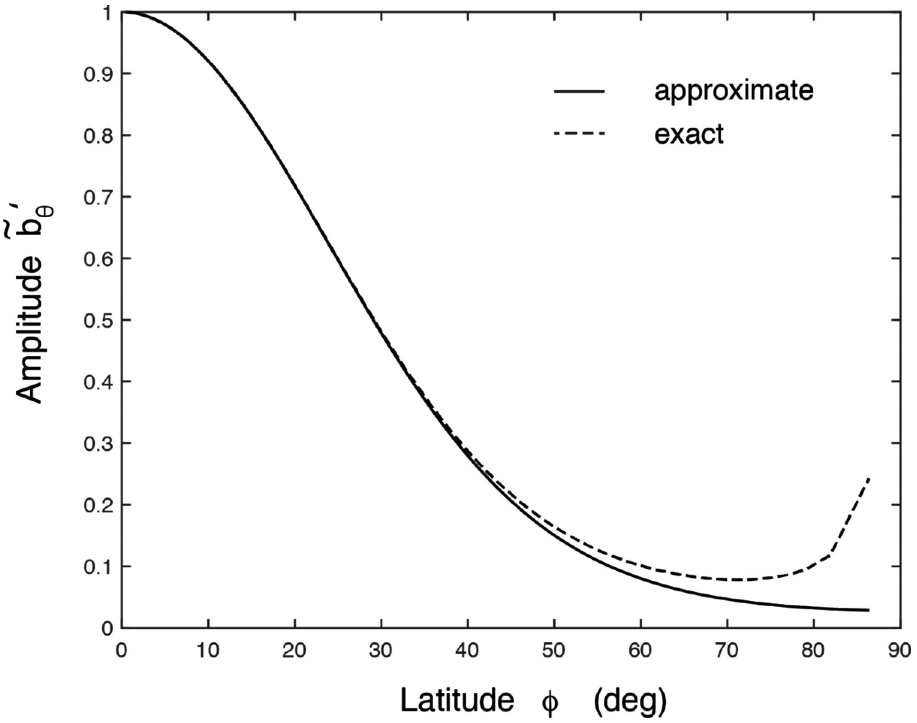

Figure 6. Amplitude of low-frequency eMAC waves computed using a constant M on the extended beta-plane. The eigenfunction, $\tilde{b}'_\theta$, is computed from $\tilde{b}''_\theta$ using the approximate (solid) and exact (dashed) transformation. Errors near the north pole arise when the exact transformation is used with an incomplete description of the spherical geometry on the extended beta-plane. These errors are reduced by using the approximate transformation. There is little difference in the structure of the wave near the equator.

We quantify the resulting error by comparing the results of a numerical solution (Knezek & Buffett 2018) with the predictions of the extended beta-plane approximation, truncated after y^2 and y^4 terms, respectively. Fig. 7 shows the wave periods as a function of m for the $n = 0$ and $n = 1$ waves. The $n = 0$ waves exhibit the greatest equatorial confinement, and these waves have periods that agree best with the numerical results, particularly at large m. Decreasing the value of m increases the error, although this error is always reduced by adding the y^4 terms. Larger errors occur for the $n = 1$ waves because these waves extend further from the equator. The magnitude of this error is reduced at large m, and the addition of y^4 terms always improves the solution. The constant M case poses the greatest challenge for the extended beta plane because the equatorial confinement of the waves is due entirely to the influence of spherical geometry. (Recall that equatorial waves are not predicted on the standard beta plane with constant M). Allowing for gradients in the radial magnetic field causes greater confinement of the waves to the equator and reduces the need for higher terms in the series expansion (see the next section).

3.4 Influence of spherical geometry and magnetic-field gradients

The results of the previous section show that eMAC waves are trapped to the equator by the effects of spherical geometry, even when the radial magnetic field is constant. The origin of this trapping was attributed to the appearance of the $2(m^2 - 1)$ term in the definition of α_2. Increasing m is expected to increase the equatorial confinement. Further increases in confinement are possible in the presence of gradients in the radial magnetic field. Retaining the influences of both spherical geometry and magnetic-field gradients complicates the algebra, but the general procedure is the same. We combine (16) and (17) to obtain a single differential equation for $\tilde{b}'_\theta$. When M is allowed to vary y according to (31), we obtain

$$(1-y^2)\partial_y^2\tilde{b}'_\theta - 2y\left[\frac{1-\Lambda^2+2\Lambda^2y^2}{1+\Lambda^2y^2}\right]\partial_y\tilde{b}'_\theta + \left[\frac{C^2y^2}{M(y)} + \frac{mC}{M(y)} - \frac{m^2}{1-y^2}\right]\tilde{b}'_\theta = 0 \quad (44)$$

after dropping small terms with $M/m^2 < <1$. Normalizing (44) using the transformation

$$\tilde{b}'_\theta = \frac{\tilde{b}''_\theta}{\sqrt{(1-y^2)(1+\Lambda^2y^2)}} \quad (45)$$

allows the differential equation for $\tilde{b}''_\theta$ to be written as

$$\partial_y^2\tilde{b}''_\theta - (\alpha_2 y^2 - \alpha_0)\tilde{b}''_\theta, \quad (46)$$

where the coefficients are

$$\alpha_0 = \frac{mC}{M(0)} - (m^2-1) - \Lambda^2 \quad (47)$$

$$\alpha_2 = -\frac{C^2}{M(0)} - \frac{mC}{M(0)}(1-\Lambda^2) + 2(m^2-1) - 2\Lambda^2(\Lambda^2+1). \quad (48)$$

Note that these coefficients revert to their previous definitions in (42) when $\Lambda = 0$.

Eq. (46) is solved as an eigenvalue problem for α_0. The recovered value is compared with the definition of α_0 in (48) to evaluate the wave frequency. The eigenfunction for $\tilde{b}''_\theta$ is transformed to $\tilde{b}'_\theta$ using (45), and back to the original magnetic perturbation $\tilde{b}_\theta$ using (13). Fig. 8 shows the first two eMAC waves, computed using $H = 100\,\text{km}$, $N = \Omega$, $Br(0) = 0.48\,\text{mT}$ and $\Lambda^2 = 2.5$. Both of

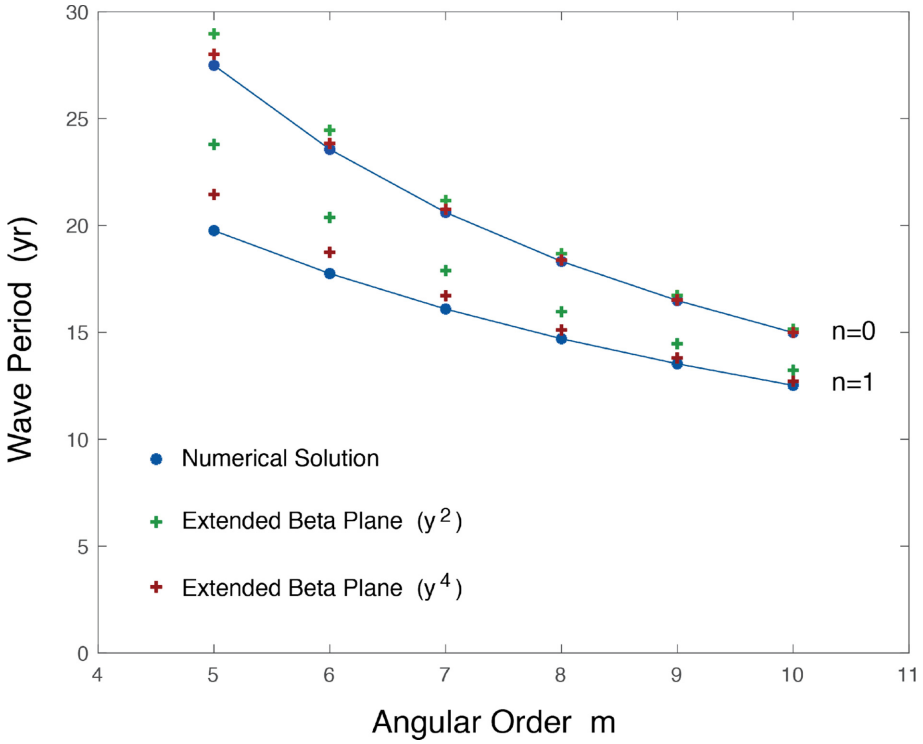

Figure 7. Period of symmetric ($n = 0$) and asymmetric ($n = 1$) waves as a function of angular order m. The numerical solution is based on the model of Knezek & Buffett (2018), whereas the two extended beta-plane solutions retain all y^2 (green) and y^4 (red) terms. Including y^4 terms improves the accuracy of the extended beta plane, although large errors remain at small m because the waves are not tightly confined to the equator. Allowing for gradients in the radial magnetic field increases the equatorial confinement and reduces the need for higher order terms in the power series. Parameters used in the calculations include $H = 40$ km, $B_r = 0.65$ mT and $N = 10\,\Omega$.

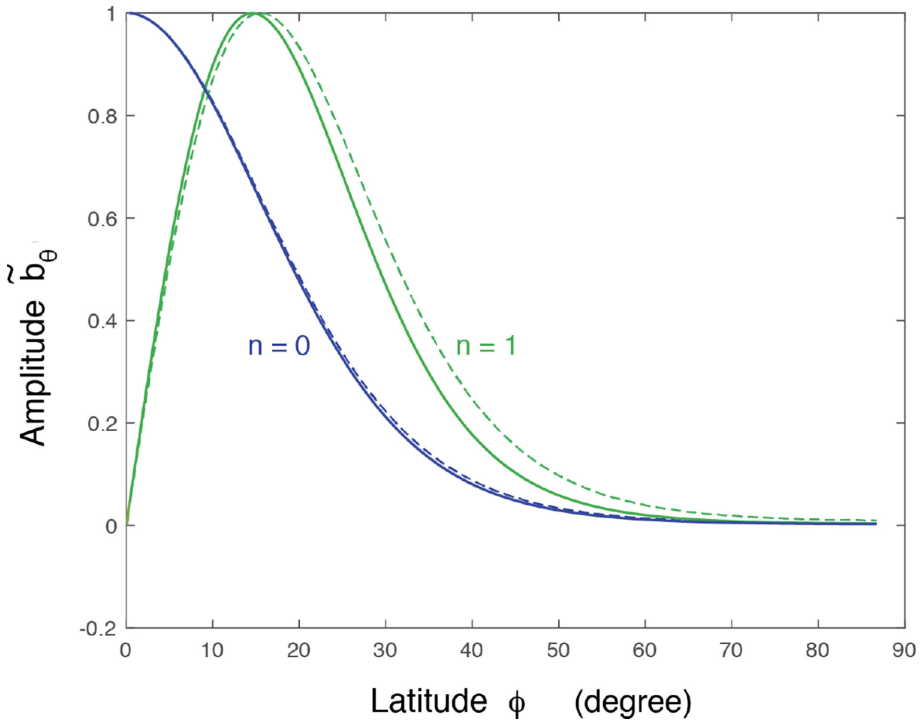

Figure 8. Amplitude of low-frequency eMAC waves on a sphere (solid lines). The combined effects of spherical geometry and magnetic-field gradients confine the waves to the equator. A solution on the standard beta-plane with the same magnetic-field gradient (dashed lines) exhibits only small differences (see the text).

these waves propagate eastwards with periods of 198.2 yr (for $n = 0$) and 127.6 yr (for $n = 1$). These periods are not substantially different from the values computed on the standard beta plane, which gave periods of 197.1 and 122.9 yr. Even the eigenfunctions are quite similar to those computed on the standard beta-plane (see Fig. 8). The eigenfunctions for the $n = 0$ wave are most similar because these waves have the greatest confinement to the equator. By comparison the $n = 1$ wave extends further from the equator, so the influences of spherical geometry are somewhat larger. In both cases we find that the influence of spherical geometry shifts the eigenfunctions towards the equator, relative to the standard beta-plane approximation. However, the overall change is small. We attribute this small change to the magnetic gradient ($\Lambda^2 = 2.5$) used in the calculation. A weaker gradient in the magnetic field (say $\Lambda^2 = 1$) allows MAC waves on the standard beta-plane to extend beyond the poles. In this case the effects of spherical geometry produce a larger change in the eigenfunctions.

4 IMPLICATIONS FOR GEOMAGNETIC ACCELERATION

Can low-frequency eMAC waves account for geomagnetic acceleration in the equatorial region? We have previously seen that waves in a thick layer ($H \approx 100$ km) have periods of roughly 200 yr for $m = 6$ and $n = 0$. The corresponding phase velocity, $\omega R/m$, is 0.6 mm s^{-1}, which is comparable to the high end of the fluid velocities inferred from secular variation (Holme 2015). When velocities for the wave and the background flow are similar, we might expect a superposition of an eastward propagating eMAC wave and a westward equatorial flow (e.g. Kloss & Finlay 2019) to produce a standing wave in observations of geomagnetic acceleration. However, the period of this oscillation would be much longer than the short-period fluctuations detected in the observations (Chulliat & Maus 2014). The question here is whether eMAC waves can have periods and spatial structures similar to that suggested by the observations.

4.1 Estimates of wave period

Waves with short periods require different conditions near the core–mantle boundary. The most effective way to lower the wave period at a fixed m is by reducing the layer thickness. Fig. 9 shows a plot of the wave period as a function of layer thickness for waves at $m = 6$ and $m = 8$. All of these waves have periods below 10 yr once the layer thickness decreases to 20 km. There is little influence of inertia, even in the thinest layers, because the transition period for inertial effects drops sharply with the layer thickness. By the time the layer thickness is reduced to 20 km ($k = \pi/H$), the transition period has decreased to 0.28 yr, which is short compared with the wave periods.

The strength of fluid stratification, N, has surprisingly little influence on the wave periods once N exceeds a threshold value. This threshold defines the condition needed for equatorially trapped waves. Numerical calculations using the extended beta plane show that the required stratification depends on the layer thickness. We have already seen that equatorial waves are predicted in a layer with $H = 100$ km when $N = \Omega$. However, a stronger stratification, $N \approx 5\Omega$, is required when H decreases to 20 km. The results shown in Fig. 9 are calculated with $N = 10\Omega$ to put these waves well into the trapped regime. Increasing the stratification to $N = 20\Omega$ decreases the periods by only 1 per cent. This means that eMAC waves are insensitive to stratification once the condition for equatorial trapping is satisfied.

A nearly quadratic dependence of the wave period on the layer thickness means that the restoring force increases as the layer becomes thinner. A similar dependence is expected for the effects of magnetic diffusion. As a result, the quality factor for these waves,

$$Q = \frac{\mathrm{Re}(\omega)}{2\,\mathrm{Im}(\omega)}, \tag{49}$$

is nearly independent of H. The waves shown in Fig. 9 have a low quality factor ($Q = 0.65$ to 1.2), and these values are nearly invariant as H is varied from 20 to 120 km. Higher quality waves are expected at higher m, but these waves are more difficult to detect in observations due to the short wavelength. Such low Q waves do not propagate very far before they are dissipated by ohmic losses. This behaviour is compatible with short-lived disturbances in geomagnetic acceleration. As an illustrative example we consider the $m = 6$ and $n = 1$ wave in a layer with $H = 20$ km. The period of this wave is 5.4 yr, whereas the quality factor is $Q = 1.0$. The phase velocity is roughly 670 km yr^{-1}, but the e-folding time for the wave amplitude is only 1.75 yr. Consequently, these waves travel only 2400 km over two e-folding times before they are effectively dissipated. This travel distance corresponds to a change in longitude of about 40 degrees. Even though waves can propagate much faster than typical fluid velocities, their lifetimes and travel distances are relatively short.

A thin layer with strong stratification is favoured to interpret short-period geomagnetic acceleration in terms of eMAC waves. By comparison, a thicker layer ($H = 140$ km) and a weaker stratification ($N = 0.84\,\Omega$) have been proposed to account for dipole fluctuations due to zonal MAC waves (Buffett *et al.* 2016). eMAC waves should still be present in the thicker layer, but their periods are too long to be detected in the relatively short record of satellite observations. Instead, we require a sublayer within the broader region of stratification to account for short-period disturbances. Such a sublayer is physically plausible because the influence of barodiffusion allows light elements to accumulate at the core–mantle boundary once a thicker layer of stratification inhibits mixing near the boundary (Buffett & Seagle 2010; Gubbins & Davies 2013). Previous calculations (Knezek & Buffett 2018) have shown that a thin layer of strong stratification within a broader layer does not substantially alter the structure and periods of zonal MAC waves. However, it is less clear whether eMAC waves in a thin stratified layer are affected by weaker stratification below the layer. Another question concerns the mechanisms needed to generate these waves. We return to these questions in Section 5.

4.2 Spatial structure of the wave velocity

Once a solution is obtained for the transformed magnetic perturbation, $\tilde{b}''_\theta$, it is straightforward to recover the other perturbations. Estimates for the wave velocity at the core–mantle boundary can be used to predict the long wavelength fluctuations in the radial magnetic field. This component of the magnetic perturbation has little influence on the dynamics, but it can be viewed as a passive tracer for the wave motion. Detectable changes in the magnetic perturbation at the surface are confined to low-degree spherical harmonics, so it is simplest to compute the radial magnetic perturbation using the wave velocity together with the observed, long-wavelength main magnetic field. To illustrate the general approach, we consider the combined influence of spherical geometry and magnetic-field

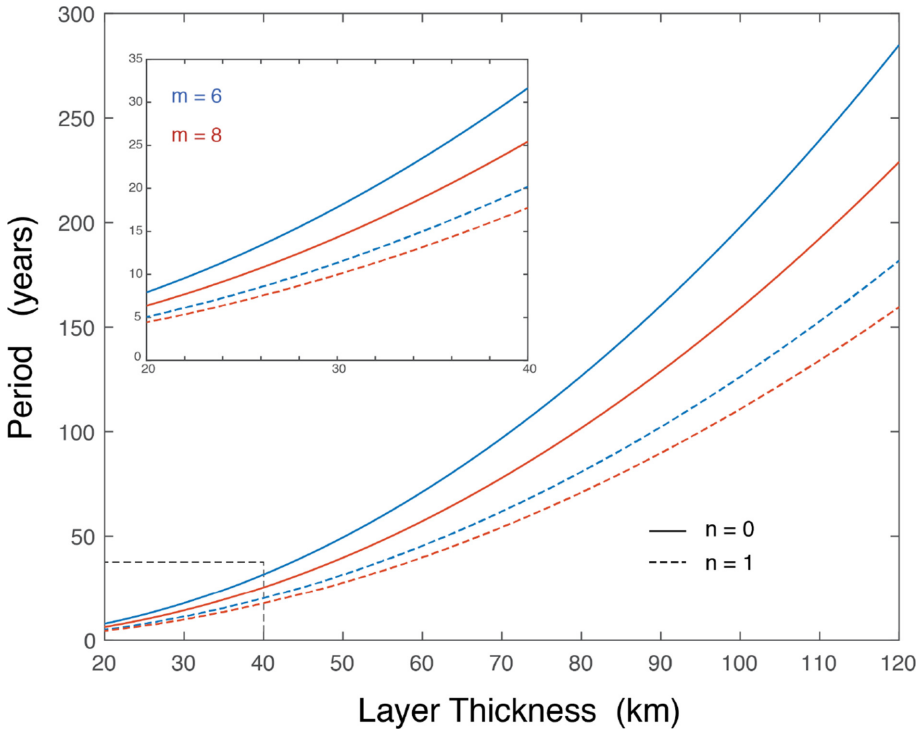

Figure 9. Dependence of wave period on layer thickness H for waves at $m = 6$ (blue) and $m = 8$ (red). Thin layers (inset) yield wave periods below 10 yr. The quality factor, Q, does not vary with H because the restoring force and the damping due to ohmic losses have a common dependence on H^2.

gradients from Section 3.4. The transformation in (45) is used to evaluate $\tilde{b}'_\theta$ and (17) is then used to compute $\tilde{b}'_\lambda$. The original magnetic perturbation is recovered using (13). A solution for the velocity perturbation can be computed from the induction equation. From the Appendix, we have

$$\partial_z v_\theta = -i\omega\chi b_\theta / B_r \tag{50}$$

for the θ component. A similar expression holds for the λ component. Here χ was defined in (21) to account for the influence of magnetic diffusion. Using the known vertical dependence of b_θ and b_λ from (14) and (15), we integrate (50) to obtain

$$\begin{aligned} v_\theta &= -\frac{i\omega\chi\tilde{b}_\theta}{B_r} e^{i(m\lambda-\omega t)} \int_{-H}^{z} \sin(kz)\,\mathrm{d}z \\ &= \frac{i\omega\chi}{k}\frac{\tilde{b}_\theta}{B_r}[1+\cos(kz)]e^{i(m\lambda-\omega t)}, \end{aligned} \tag{51}$$

where we have used the boundary condition $v_\theta = 0$ at $z = -H$.

Fig. 10 shows the velocity field at the core–mantle boundary ($z = 0$) for the first two eMAC waves at $m = 8$. The magnitude and direction of flow is represented using arrows, while the shading indicates the horizontal divergence (red for positive and blue for negative). The $n = 0$ wave predicts flow across the equator, whereas the $n = 1$ wave yields symmetric flow on either side of the equator. The latter wave ($n = 1$) appears to be more consistent with recent estimates of flow in the equatorial region (Kloss & Finlay 2019).

The amplitude of the flow is not specified by the eigenvalue problem, but the relative magnitudes of the velocity, acceleration and horizontal divergence are established by the calculation. As an example, we consider the $n = 1$ wave in a 20 km layer; the wave period at $m = 8$ is 4.6 yr. Adopting a flow velocity of 5 km yr^{-1} gives an acceleration of 6.8 km yr^{-2}, which is comparable to estimates from Kloss & Finlay (2019). However, the estimates for horizontal divergence differ by roughly order of magnitude. The eMAC wave gives a horizontal divergence of 0.6×10^{-3} yr^{-1}, whereas Kloss & Finlay (2019) recover a value of roughly 10^{-2} yr^{-1}. The difference is partially related to the way that the velocity field is represented by Kloss & Finlay (2019). Time-dependent flow is expressed in the form of low-frequency inertial waves, which allow greater horizontal divergence compared with eMAC waves. Whether the greater horizontal divergence is required to account for observations of geomagnetic acceleration is not clear because the spatial structure of the flow is set by the form of the inertial waves. For that reason it would be of interest to assess whether a flow structure based on eMAC waves can also offer a viable description of geomagnetic acceleration.

5 DETECTING WAVES IN GEOMAGNETIC ACCELERATION

Short-period waves in a thin layer of stratified fluid at the top of the core can produce the correct range of timescales for fluctuations in geomagnetic acceleration. These waves can have periods less than 5 yr and an e-folding time of just 1–2 yr, depending on the angular order m. A large phase velocity should produce rapid variations, but the lifetime of these waves is quite short. We expect disturbances to disappear soon after they are generated. A search for eMAC waves in observations of geomagnetic acceleration would focus on eastward propagating disturbances, although it may be difficult to separate wave propagation from the generation processes. For example, a pervasive westward drift of buoyant plumes in the equatorial region (Christensen & Wicht 2015) could be responsible for generating eMAC waves, either through the influence of buoyant fluid rising into the stratified layer, or more likely, through magnetic disturbances at the base of the layer (Aubert 2018). A westward drift

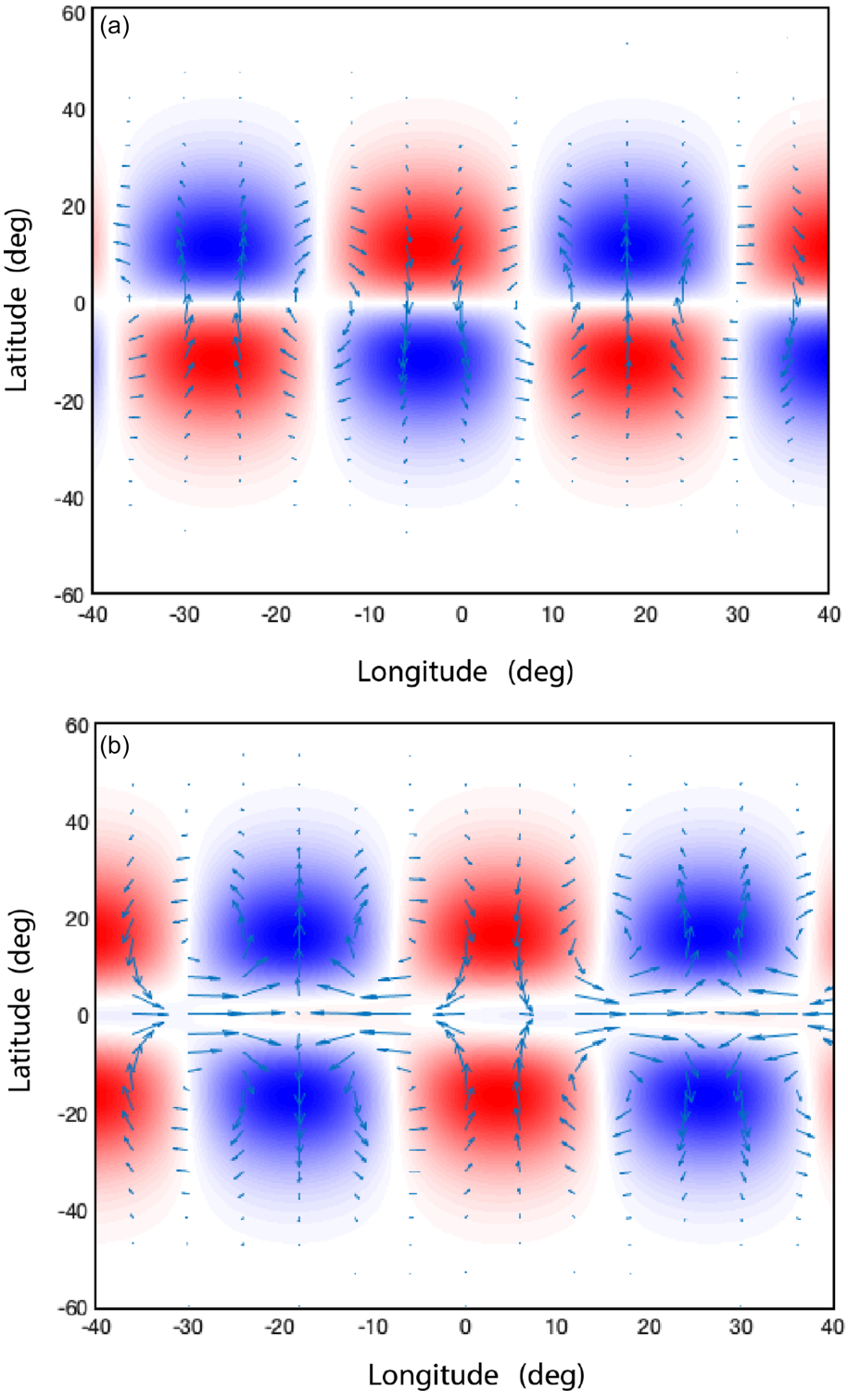

Figure 10. Horizontal flow at the core–mantle boundary due to a $n = 0$ wave (a) and $n = 1$ wave (b). Arrows represent the direction and amplitude of flow, while the shading indicates horizontal divergence in the velocity (red for positive and blue for negative). The symmetry of the wave amplitude, $\tilde{b}_\theta$, is opposite to the symmetry of the flow. Asymmetric flow about the equator is produced by the $n = 0$ wave and symmetric flow occurs for the $n = 1$ wave.

of the source mechanism might drive pulses of geomagnetic acceleration that migrate to the west, even though the waves associated with these disturbances propagate to the east.

A separation of the source mechanism from the wave propagation may be possible if the cause of eastward propagating disturbances is due mainly to wave motion. By computing the flow associated with eMAC waves for a wide range of conditions, we can produce a suite of forward models for the expected geomagnetic acceleration. Detailed predictions would rely on the computed wave motion to advect the observed long-wavelength structure of the main magnetic field (Finlay *et al.* 2016; Barrois *et al.* 2018). We would then search for correlations with the observed geomagnetic acceleration (Knezek

& Buffett 2019). The spatial and temporal limits on the correlation would be set by the structure and damping time of the waves. Even if a large part of the geomagnetic acceleration is due to a westward migration of the wave source, a persistent eastward propagating component should be present in the observations if the waves exist. Detecting these waves would provide valuable constraints on the evolution of conditions near the core–mantle boundary, including the duration of sublayer growth through barodiffusion. The simplicity and low-computational cost of the model developed in this study enables a very efficient forward model for comparison with observations of geomagnetic acceleration.

6 CONCLUSIONS

We develop a physical model for equatorially trapped waves with the goal of interpreting observations of rapid fluctuations in geomagnetic acceleration. Westward propagating magnetic Rossby waves are predicted on the standard beta plane when the rms radial magnetic field is constant over the surface of the core–mantle boundary. Gradients in the Coriolis force away from the equator alter the local wave speed, creating a wave guide for magnetic Rossby waves. These waves have periods of weeks to months, which is probably too short to be detected in geomagnetic acceleration.

Low-frequency waves in the equatorial region are not expected on the standard beta-plane when the rms radial magnetic field is constant. However, eastward propagating MAC waves become trapped near the equator when the magnetic force increases away from the equator. This gradient in the magnetic force produces a wave guide in much the same way as a gradient in the Coriolis force creates a wave guide for magnetic Rossby waves. Representative gradients in the magnetic force from a geodynamo model are sufficient to localize MAC waves to the equator. Equatorially trapped MAC waves are also predicted in the presence of a weak magnetic gradient when we account for the influences of spherical geometry.

An extension of the standard beta-plane approximation to account for the influences of spherical geometry is based on a power series expansion in the meridional coordinate, $y = \cos\theta$, where θ is co-latitude. Retaining only the second-order terms in y is often sufficient to give good agreement with a prior numerical model (Knezek & Buffett 2018). However, the current model is computationally more efficient. This efficiency makes it feasible to use the extended beta-plane as a forward model for predicting fluctuations in geomagnetic acceleration. By searching for a significant correlation between these predictions and the observed geomagnetic acceleration, we can seek to detect low-frequency MAC waves and constrain the physical conditions that support these waves.

ACKNOWLEDGEMENTS

This project was supported by the National Science Foundation (EAR-1430526) and by an award from the Department of Energy INCITE Program. We thank the Computational Infrastructure for Geodynamics (CIG), which is funded by the National Science Foundation under awards EAR-0949446 and EAR-1550901. The numerical solution used in this study was run by Rakesh Yadav on supercomputers at the Argonne National Laboratory. We thank two reviewers for thoughtful comments and suggestions.

REFERENCES

Aubert, J., 2018. Geomagnetic acceleration and rapid hydromagnetic wave dynamics in advanced numerical simulations of the geodynamo, *Geophys. J. Int.,* **214,** 531–547.

Bäerenzung, J., Holschneider, M., Wicht, J., Sanchez, S. & Lesur, V., 2018. Modeling and predicting the short-period evolution of the geomagnetic field, *J. geophys. Res.,* **123,** 4539–4560.

Barrois, O., Hammer, H.D., Finlay, C.C., Martin, Y. & Gillet, N., 2018. Assimilation of ground and satellite magnetic measurements: inference of core surface magnetic and velocity field changes, *Geophys. J. Int.,* **215,** 695–712.

Bergman, M.I., 1993. Magnetic Rossby waves in a stably stratified layer near the surface of the Earth's outer core, *Geophys. Astrophys. Fluid Dyn.,* **68,** 151–176.

Braginsky, S., 1993. MAC oscillations of the hidden ocean of the core, *J. Geomag. Geoelectr.,* **48,** 1517–1538.

Buffett, B.A., 2014. Geomagnetic fluctuations reveal stable stratification at the top of the Earth's core, *Nature,* **507,** 484–487.

Buffett, B.A. & Seagle, C.T., 2010. Stratification of the top of the core due to chemical interactions with the mantle, *J. geophys. Res.,* **115,** B04407, doi:10.1029/2009JB006751.

Buffett, B.A., Mathews, P.M. & Herring, T.A., 2002. Modeling of nutation and precession: effects of electromagnetic coupling, *J. geophys. Res.,* **107**(B4), ETG 5-1-ETG 5-14.

Buffett, B.A., Knezek, N. & Holme, R., 2016. Evidence for MAC waves at the top of Earth's core and implications for variations in length of day, *Geophys. J. Int.,* **204,** 1789–1800.

Canet, E., Finlay, C. & Fournier, A., 2014. Hydromagnetic quasi-geostrophic models of the geomagnetic secular variation, *Phys. Earth planet. Inter.,* **229,** 1–15.

Christensen, U.R. & Aubert, J., 2006. Scaling properties of convection-driven dynamos in rotating spherical shells and application to planetary magnetic fields, *Geophys. J. Int.,* **166,** 97–114.

Christensen, U.R. & Wicht, J., 2015. Numerical dyanmo simulations, in Treatise on Geophysics, Vol. 8, pp. 245–277, Elsevier.

Chulliat, A. & Maus, S., 2014. Geomagnetic secular acceleration, jerks, and a localized standing wave at the core surface from 2000 to 2010, *J. geophys. Res.,* **119,** 1531–1543.

Chulliat, A., Thebault, E. & Hulot, G., 2010. Core field acceleration pulse as a common cause of the 2003 and 2007 geomagnetic jerks, *Geophys. Res. Lett.,* **37,** L07301, doi:10.1029/2009GL042019

Chulliat, A., Alken, P. & Maus, S., 2015. Fast equatorial waves propagating at the top of the Earth's core, *Geophys. Res. Lett.,* **42,** 3321–3329.

de Wijs, G.A., Kresse, G., Vocadlo, L., Dobson, D., Alfe, Gillian, M.J. & Price, G.D., 1998. The viscosity of liquid iron at the physical conditions of the Earth's core, *Nature,* **393,** 805–807.

Featherstone, N.A. & Hindman, B.W., 2016. The spectral amplitude of stellar convection and its scaling in the high-Rayleigh-number regime, *Astrophys. J.,* **818,** 32.

Finlay, C.C. & Jackson, A., 2003. Equatorially dominated magnetic field change at the surface of Earth's core, *Science,* **300,** 2084–2086.

Finlay, C.C., Olsen, N., Kotsiaros, S., Gillet, N. & Toeffner-Clausen, L., 2016. Recent geomagnetic secular variation from Swarm and ground observatories as estimated in the CHAOS-6 geomagnetic field model, *Earth Planets Space,* **68**(112), doi:10.1186/s40623-016-0486-1.

Gubbins, D. & Davies, C.J., 2013. The stratified layer at the core-mantle boundary by barodiffusion of oxygen, sulphur and silicon, *Phys. Earth planet. Inter.,* **215,** 21–28.

Holme, R., 2015. Large-scale flow in the core, in *Treatise on Geophysics,* 2nd ed., Vol. **8,** pp. 91–113, Elsevier.

Hori, K., Jones, C.A. & Teed, R.J., 2015. Slow magnetic Rossby waves in the Earth's core, *Geophys. Res. Lett.,* **42,** 6222–6629.

Ichikawa, H. & Tsuchiya, T., 2015. Atomic transport properties of Fe-O liquid alloys in the Earth's outer core P, T condition, *Phys. Earth planet. Inter.,* **247,** 27–35.

Jackson, A., 1997. Time dependency of tangentially geostrophic core surface motion, *Phys. Earth planet. Inter.,* **103,** 293–311.

Jackson, A., Bloxham, J. & Gubbins, D., 1993. Time-dependent flow at the core surface and conservation of angular momentum in the coupled core-mantle system, in *Dynamics of Earth's Deep Interior and Earth's Rotation,* Vol. **72,** pp. 97–107, eds Le Mouël J.-L., Smylie D.E., Herring T., American Geophysical Union Monograph.

Jackson, A., Jonkers, A.R.T. & Walker, M.R., 2000. Four centuries of geomagnetic secular variation from historical records, *Phil. Trans. R. Soc. Lond. A,* **358,** 957–990.

Jault, D., Gire, C. & LeMouël, J.-L., 1988. Westward drift, core motions and exchanges of angular momentum between core and mantle, *Nature,* **333,** 353–356.

Kloss, C. & Finlay, C.C., 2019. Time-dependent low latitude core flow and geomagnetic field acceleration pulses, *Geophys. J. Int.,* **218,** 140–168.

Knezek, N. & Buffett, B., 2018. Influence of magnetic field configuration on magnetohydrodynamic waves in Earth's core, *Phys. Earth planet. Inter.,* **277,** 1–9.

Knezek, N. & Buffett, B., 2019. Extracting waves from noisy geomagnetic data - a synthetic study of equatorially trapped waves in Earth's core, *Phys. Earth planet. Inter.,* **286,** 81–91.

Koot, L., Dumberry, M., Rivoldini, A., de Viron, O. & Dehant, V., 2010. Constraints on the coupling at the core-mantle and inner core boundaries inferred from nutation observations, *Geophys. J. Int.,* **182,** 1279–1294.

Labbe, F., Jault, D. & Gillet, N., 2015. On magnetostrophic inertia-less waves in quasi-geostrophic models of planetary cores, *Geophys. Astrophys. Fluid Dyn.,* **109,** 587–610.

Lanczos, C., 1996, *Linear Differential Operators,* SIAM Publications.

Lesur, V., Wardinski, I., Rother, M. & Mandea, M., 2008. GRIMM: the GFZ reference internal magnetic model based on vector satellite and observatory data, *Geophys. J. Int.,* **173,** 382–394.

Marquez-Artavia, X., Jones, C.A. & Tobias, S.M., 2017. Rotating magnetic shallow water waves and instabilities, *Geophys. Astrophys. Fluid Dyn.,* **111,** 282–322.

Matsui, H. *et al.*, 2016. Performance benchmark for a next generation numerical dynamo model, *Geochem. Geophys. Geosys.,* **17,** 1586–1607.

Olsen, N., Luhr, H., Sabaka, T.J., Mandea, M., Rother, M., Tofner-Clausen, L. & Choi, S., 2006. CHAOS - a model of the Earth's magnetic field derived from CHAMP, Orsted, and SAC-C magnetic satellite data, *Geophys. J. Int.,* **166,** 67–75.

Pedlosky, J., 1987. *Geophysical Fluid Dynamics,* 2nd Edition, Springer.

Pedlosky, J., 2003. Equatorial beta-plane and equatorial waves, in *Waves in the Ocean and Atmophere,* Vol. **18,** pp. 193–204, Springer.

Zaqarashvili, T.V., Oliver, R., Ballester, J.L. & Shergelashvili, B.M., 2007. Rossby waves in shallow water magnetohydrodynamics, *Astron. Astrophys.,* **470,** 815–820.

APPENDIX A: AN EXTENDED BETA-PLANE FOR EQUATORIALLY TRAPPED WAVES

Equatorial waves are expressed in terms perturbations in velocity, **v**, magnetic field **b**, density ρ_1 and pressure p. The time dependence of these perturbations is described by the momentum, magnetic induction and the conservation of mass equations. Section 2 gives the specific form of these equations in spherical coordinates (r, θ, λ). The goal of this Appendix is to successively eliminate individual perturbations from the governing equations to obtain a pair of equations for the horizontal components of the magnetic perturbation, b_θ and b_λ. These equations serve as the starting point for the extended beta-plane approximation.

We begin with the spherical components of the momentum equation in (5)–(7). The radial force balance is assumed to be hydrostatic, so we eliminate the pressure perturbation by differentiating the $\hat{\theta}$ and $\hat{\lambda}$ components of the momentum equation with respect to radius and use the hydrostatic balance to replace pressure with the density perturbation. The result is

$$\partial_r \partial_t v_\theta - 2f\partial_r v_\lambda = \frac{1}{\rho_0 R}\partial_\theta(\rho_1 g) + \frac{1}{\rho_0 \mu} B_r \partial_r^2 b_\theta, \tag{A1}$$

$$\partial_r \partial_t v_\lambda + 2f\partial_r v_\theta = \frac{1}{\rho_0 R \sin\theta}\partial_\lambda(\rho_1 g) + \frac{1}{\rho_0 \mu} B_r \partial_r^2 b_\lambda, \tag{A2}$$

where $f = 2\Omega\cos\theta$ is the Coriolis parameter.

Next we eliminate ρ_1 using conservation of mass in (2). Differentiating (A1) and (A2) with respect to time and substituting for $\partial_t \rho_1$ from (2) gives

$$\partial_r \partial_t^2 v_\theta - 2f\partial_r \partial_t v_\lambda = \frac{N^2}{R}\partial_\theta v_r + \frac{1}{\rho_0 \mu} B_r \partial_r^2 \partial_t b_\theta \tag{A3}$$

$$\partial_r \partial_t^2 v_\lambda + 2f\partial_r \partial_t v_\theta = \frac{N^2}{R\sin\theta}\partial_\lambda v_r + \frac{1}{\rho_0 \mu} B_r \partial_r^2 \partial_t b_\lambda, \tag{A4}$$

where the (squared) buoyancy frequency

$$N^2 = -\frac{g}{\rho_0}\frac{\partial \rho_0}{\partial r} \tag{A5}$$

is assumed to be independent of θ and λ.

The radial velocity is eliminated using the continuity condition, $\nabla \cdot \mathbf{v} = 0$, which can be approximated in a thin spherical shell as

$$\partial_r v_r = -\frac{1}{R\sin\theta}\partial_\theta(v_\theta \sin\theta) - \frac{1}{R\sin\theta}\partial_\lambda v_\lambda. \tag{A6}$$

Introducing a change of variable $y = \cos\theta$ allows us to write the continuity equation in the form

$$\partial_r v_r = \frac{1}{R}\left[\partial_y v'_\theta - \partial_\lambda v'_\lambda\right], \tag{A7}$$

where

$$v'_\theta = v_\theta(1-y^2)^{1/2},\ v'_\lambda = v_\lambda(1-y^2)^{-1/2}. \tag{A8}$$

These modified velocity perturbations are completely analogous to the modified magnetic perturbations (b'_θ, b'_λ) in (13). Differentiating (A3) and (A4) with respect to r, and using the continuity equation to eliminate $\partial_r v_r$, gives

$$\partial_r^2 \partial_t^2 [v'_\theta(1-y^2)^{-1}] - 2\Omega y \partial_r^2 \partial_t v'_\lambda = -\frac{N^2}{R^2}\partial_y[\partial_y v'_\theta - \partial_\lambda v'_\lambda] + \frac{B_r}{\rho_0 \mu}\partial_r^3 \partial_t [b'_\theta(1-y^2)^{-1}] \tag{A9}$$

$$\partial_r^2 \partial_t^2 [v'_\lambda(1-y^2)] + 2\Omega y \partial_r^2 \partial_t v'_\theta = \frac{N^2}{R^2}\partial_\lambda[\partial_y v'_\theta - \partial_\lambda v'_\lambda] + \frac{B_r}{\rho_0 \mu}\partial_r^3 \partial_t [b'_\lambda(1-y^2)], \tag{A10}$$

where we assume that N^2 does not vary with radius. We also introduce the modified magnetic perturbations, b'_θ and b'_λ, from (13).

The final step is to eliminate the velocity perturbations using the magnetic induction equation in (8). The $\hat{\theta}$ and $\hat{\lambda}$ components of the induction equation are

$$B_r \partial_r v_\theta = (\partial_t - \eta \partial_r^2) b_\theta, \tag{A11}$$

$$B_r \partial_r v_\lambda = (\partial_t - \eta \partial_r^2) b_\lambda, \tag{A12}$$

although an identical relationship also holds between the modified velocity and magnetic perturbations. Introducing the vertical coordinate $z = r - R$, and substituting the assumed form of the solution for b'_θ and b'_λ from (14) and (15) gives

$$\partial_z v'_\theta = -i\omega\chi b'_\theta / B_r, \tag{A13}$$

$$\partial_z v'_\lambda = -i\omega\chi b'_\lambda / B_r, \tag{A14}$$

where

$$\chi = 1 + \frac{i\eta k^2}{\omega}. \tag{A15}$$

Differentiating (A9) and (A10) with respect to z, and using (A13) and (A14) to eliminate the modified velocity perturbation, gives the final form of the equations for the coefficients $\tilde{b}'_\theta(y)$ and $\tilde{b}'_\lambda(y)$ in (16) and (17).